



HAL
open science

Model reduction techniques for quantitative nano-mechanical AFM mode

Xuyang Chang, Stéphane Roux, Simon Hallais, Kostas Danas

► **To cite this version:**

Xuyang Chang, Stéphane Roux, Simon Hallais, Kostas Danas. Model reduction techniques for quantitative nano-mechanical AFM mode. Measurement Science and Technology, In press. hal-03174330

HAL Id: hal-03174330

<https://hal.science/hal-03174330>

Submitted on 19 Mar 2021

HAL is a multi-disciplinary open access archive for the deposit and dissemination of scientific research documents, whether they are published or not. The documents may come from teaching and research institutions in France or abroad, or from public or private research centers.

L'archive ouverte pluridisciplinaire **HAL**, est destinée au dépôt et à la diffusion de documents scientifiques de niveau recherche, publiés ou non, émanant des établissements d'enseignement et de recherche français ou étrangers, des laboratoires publics ou privés.

1 Model reduction techniques for quantitative 2 nano-mechanical AFM mode

3 **X. Chang¹, S. Hallais¹, S. Roux² and K. Danas¹**

4 ¹LMS, C.N.R.S, École Polytechnique, Institut Polytechnique de Paris,
5 91128 Palaiseau, France

6 ² Université Paris-Saclay/ENS Paris-Saclay/C.N.R.S.,
7 LMT - Laboratoire de Mécanique et Technologie, 91190 Gif-sur-Yvette, France

8 E-mail: konstantinos.danas@polytechnique.edu

9 December 2020

10 **Abstract.** A recently developed atomic force microscope (AFM) process, the Peak-
11 Force Quantitative Nanomechanical Mapping (PF-QNM) mode, allows to probe over a
12 large spatial region surface topography together with a variety of mechanical properties
13 (*e.g.* apparent modulus, adhesion, viscosity). The resulting large set of data often
14 exhibits strong coupling between material response and surface topography. This letter
15 proposes the use of a proper orthogonal decomposition (POD) technique to analyze
16 and segment the force-indentation data obtained by the PF-QNM mode in a highly
17 efficient and robust manner. Two samples illustrate the proposed methodology. In
18 the first one, low density polyethylene nanopods are deposited on a polystyrene film.
19 The second is made of carbonyl iron particles embedded in a polydimethylsiloxane
20 matrix. The proposed POD method permits to seamlessly identify the underlying
21 phase constituents in both samples and decouple them from the surface topography
22 by compressing voluminous force-indentation data into a subset with a much lower
23 dimensionality.

24 *Keywords* : AFM; PeakForce-QNM; Segmentation; Model reduction technique; POD

25
26 Submitted to: *Meas. Sci. Technol.*

1. Introduction

Since Scanning Force Microscopy (SFM, aka SPM) was introduced [1], AFM has evolved into one of the most powerful tools for surface characterization [2]. Various new AFM modes has been proposed to provide local material properties together with topography with a high scanning rate (*e.g.*, Tapping Mode [3], Pulse force Mode [4, 5], Contact Resonance-AFM [6] and etc). Peak-Force Quantitative Nanomechanical Mapping (PF-QNM) AFM mode has been introduced [7] as a new extension of previous Pulse Force AFM mode, aiming to robustly explore simultaneously various nanoscale mechanical properties [8–11]. By monitoring the instantaneous deflection of the cantilever, a continuous feedback loop is implemented to control the force between the tip and sample [12, 13]. Force-indentation curves are generated separately for each tip oscillation (pixel by pixel) inside the region of interest (ROI), allowing to probe not only morphological properties (*e.g.* surface topography) but also various material mechanical properties such as Young’s modulus, visco-elasticity, adhesion, or any indentation related properties [14–16].

In a PF-QNM analysis or any other type of micro/nano-indentation process, the measured force-indentation data involve the combined effect of sample topography, physical and chemical material properties [17–19], as well as the effective contact area between tip and sample. For most intrinsically hard materials (*e.g.* metals and ceramics), both the indentation size effect has been well investigated [20–24] and data analysis tools to estimate a reliable Young modulus has been established [25, 26].

On the contrary, the lack of reliable nonlinear elastic contact models frequently compels the (inappropriate) use of Hertzian or Sneddon models to estimate the local apparent modulus and likely contributes to inconsistencies associated with the results of AFM measurements [27, 28]. As a result, the mere use of the sole apparent modulus is insufficient to properly segment the phases in heterogeneous samples in a PF-QNM mode [14, 27]. By contrast, use of the entire spatial and temporal force-indentation information may prove highly inefficient due to voluminous and overlapping data-sets that cannot be segmented properly and consequently lead to multiple fake material phases as a result of user-dependent segmentation processing.

From a data-mining perspective, the multi-dimensional character of the data does not allow for an intuitive and rigorous analysis [29], as compared to more classical two- and three-dimensional data spaces. In order to overcome the multi-dimensional and complex nature of the raw data obtained in a classical PF-QNM mode, it is proposed in this letter the use of a model reduction analysis such as the Proper Orthogonal Decomposition technique (POD [30] aka SVD [31] or PCA [32]). This technique allows to reorganize the data hierarchically, so that a mere truncation is a natural way to focus on the dominant features of the data-set, leaving aside higher-order information that contribute only weakly to the resulting force-indentation response at a given pixel. Furthermore, the truncation order is a choice that can be tuned if needed. This allows to clearly identify the underlying phases of the heterogeneous material and even decouple

68 them from the surface topography, which usually interferes with the measured force
 69 response. In this view, the POD truncation is an effective method to convert the
 70 voluminous data-set into a subset with a much lower dimensionality and first-order
 71 information, where relevant features can be easily observed. Note however that the
 72 proposed approach is agnostic with respect to the physics of data. This makes the
 73 method highly versatile as no prior knowledge is encoded in the method, yet, it calls
 74 for a final physical, chemical and/or mechanical interpretation of the segmented data.
 75 This latter part is beyond the scope of the present letter and is left for a future study.

76 The efficiency of the proposed methodology is illustrated by two different
 77 heterogeneous samples. The first one consists of low density polyethylene (LDPE)
 78 canonical well-shaped disks, with no overlap, deposited on a polystyrene (PS) matrix,
 79 and is used as a patch test. The second sample comprises, in turn, hard micron-
 80 sized carbonyl-iron particles (CIP) embedded into a polydimethylsiloxane (PDMS)
 81 matrix [33–36] leading to strong topography variations and non-trivial force-indentation
 82 spatial response.

83 2. PeakForce QNM mode

84 The experimental characteristics and output of the AFM PF-QNM mode are briefly
 85 described in Fig. 1. The laser spot is focused on the surface of the cantilever beam
 86 (Fig. 1a) and the associated probe measures the laser shifting voltage (LSV) over
 87 time, $\delta V(\mathbf{x}, t)$ at a given pixel on the surface described by the in-plane position
 88 vector $\mathbf{x} = (x, y)$. After a proper calibration process (usually performed on a non-
 89 deformable sapphire sample), the bending stiffness of the cantilever κ and the sensitivity
 90 of the cantilever deflection γ are estimated assuming a *linear elastic, pure-bending*
 91 response. This allows to directly associate the LSV measurement to the reaction force by
 92 $F(\mathbf{x}, t) = \kappa \delta V(\mathbf{x}, t)$ (Fig. 1b) and the cantilever deflection as $d_{\text{df}} = \gamma \delta V(\mathbf{x}, t)$ (Fig. 1c).
 93 The actual indentation depth $\delta(\mathbf{x}, t)$ of the cantilever tip is given as the difference of
 94 the prescribed vertical displacement of the cantilever Z (Fig. 1d) and the cantilever
 95 deflection as d_{df} , $\delta(\mathbf{x}, t) = Z - d_{\text{df}}$.

96 Use of δ , instead of Z or of time t , allows for the influence of topography to be erased
 97 for the most part. Fig. 1e shows a representative force-penetration, $F - \delta$, response at a
 98 fixed position (pixel) \mathbf{x} . The paths A→B→C→D (blue line) and D→E→F (red line)
 99 correspond to the loading and unloading response, respectively.

100 The entire $F - \delta$ response may then be divided in four main regimes (Fig. 1e):

101 – **Regime I: A→B→C**. As the tip approaches the surface of the specimen, an
 102 unstable jump towards contact occurs. The first force minimum during loading at
 103 B is used as a conventional *definition* of contact, and thus as an estimate of surface
 104 topography. However, because of the intrinsically unstable character of this “snap-
 105 in” and its associated hysteresis [37], this commonly adopted definition appears to be
 106 delicate, and may intermingle topography with surface force gradients. An alternative
 107 more rigorous definition of topography may be obtained with regard to point C, where

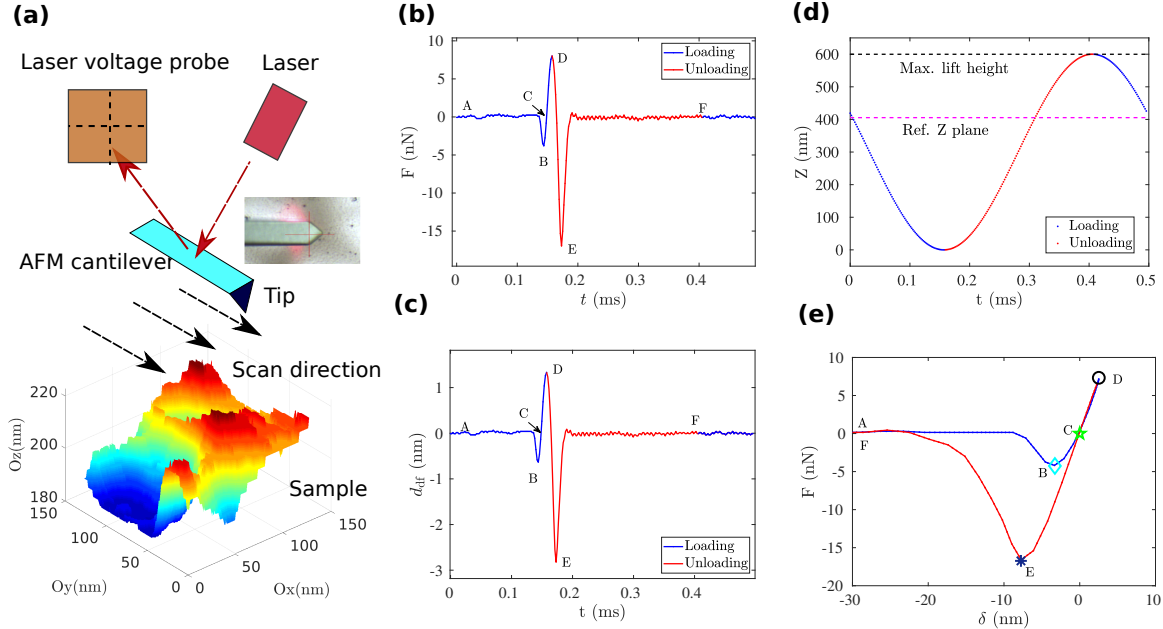


Figure 1: PeakForce QNM AFM mode. (a) AFM PeakForce QNM mode: a prescribed displacement loading is repeated in every pixel along the scanning direction; a laser beam reflected by AFM cantilever, is measured by a photo-diode delivering a laser shifting voltage (LSV), which can be converted in cantilever tip position and force at each instant in time t . (b) The deflection force F vs. time t , (c) cantilever deflection d_{df} vs. time t , (d) total vertical displacement of the cantilever Z vs. time t , (e) deflection force F vs. actual indentation depth $\delta = Z - d_{df}$. The markers denote the different regimes discussed in the main text.

108 the tip is in contact with the surface exerting a zero overall applied force. Thus the
 109 surface elevation $\delta_e(\mathbf{x})$ at a spatial point \mathbf{x} is obtained by the implicit equation

$$110 \quad F(\mathbf{x}, \delta_e(\mathbf{x})) = 0. \quad (1)$$

111 – Regime II: C→D. As the cantilever is pushed towards the surface, the force turns
 112 from attractive (before point C) to repulsive (after point C) and reaches a maximum at
 113 point D.

114 – Regime III: D→E. The tip is then withdrawn (unloading), and the response is
 115 that of a (visco)-elastic adhesive contact. Adhesion can be characterized through the
 116 pull-out force F reached at point E in the $F - \delta$ curve (dark blue star symbol).

117 – Regime IV: E→F. Complete retraction of the tip is mainly dominated by the
 118 mechanical instability of tip detachment from the surface, similar to Regime I, but with
 119 a higher amplitude because of adhesion.

120 One often assumes that the sample remains purely elastic during the unloading cycle
 121 D→E, so that an effective apparent Young’s modulus can be estimated, using either a
 122 Hertz or a Sneddon contact model. Nonetheless, if nonlinear and/or viscous effects are
 123 present, this analysis can lead to erroneous results, as is the case here especially in the
 124 second PDMS-CIP sample.

125 3. Proper Orthogonal Decomposition

126 This section discusses in some detail the proper orthogonal decomposition (POD)
 127 analysis used to analyze the force-indentation data obtained from the PF-QNM AFM
 128 mode. Initially introduced in Ref. [38] to study turbulence, the POD is a powerful
 129 and elegant method for data analysis aimed at obtaining low-dimensional approximate
 130 descriptions of a large data-set.

131 Specifically, in the present work, the force-indentation response is collected in a
 132 matrix form $\mathbf{F}(\mathbf{x}_i, \delta_j)$ written in index notation as F_{ij} . This matrix is sampled at
 133 each pixel position, \mathbf{x}_i , ($i = 1, \dots, N_x$ with N_x denoting the number of pixels) and each
 134 indentation depth, δ_j ($j = 1, \dots, N_\delta$ with N_δ denoting the dimension of the indentation
 135 discretization). It should be noted here that linear interpolation between subsequent δ_j
 136 is required in general to obtain intermediate data necessary for the subsequent processes.

The POD analysis allows then to separate the matrix \mathbf{F} into a set of orthonormal
 basis vectors (the POD modes) for representing a given data in the form

$$\mathbf{F}(\mathbf{x}, \delta) = \sum_{n=1}^{N_\delta} \lambda^{(n)} \mathbf{U}^{(n)}(\mathbf{x}) \mathbf{W}^{(n)}(\delta), \quad \text{or} \quad F_{ij} \equiv \sum_{n=1}^{N_\delta} \lambda^{(n)} U_i^{(n)} W_j^{(n)}. \quad (2)$$

137 Here, $\mathbf{W}^{(n)} \in \mathbb{R}^{N_\delta}$ represents the elementary force-indentation mode (normalized as
 138 $\|\mathbf{W}^{(n)}\| = 1$ †), $\mathbf{U}^{(n)} \in \mathbb{R}^{N_x}$ is the spatial modulation of this elementary response
 139 (normalized as $\|\mathbf{U}^{(n)}\| = 1$) and $\lambda^{(n)}$ is a global modal amplitude. At this stage, no
 140 approximation is involved, and for all data series $\mathbf{F}(\mathbf{x}, \delta)$, such an exact space-indentation
 141 decomposition always exists (but is not unique).

Then, one may easily show that both the spatial and the force modes are orthogonal,
 i.e.,

$$\mathbf{U}^{(n)} \cdot \mathbf{U}^{(m)} = \mathbf{W}^{(n)} \cdot \mathbf{W}^{(m)} = \delta^{(nm)} \quad (3)$$

with $\delta^{(nm)} = 1$ if $n = m$ and 0 otherwise. From the orthonormality conditions, the
 following relations can be readily derived

$$\lambda^{(n)} \mathbf{U}^{(n)} = \mathbf{F} \mathbf{W}^{(n)} \quad (4)$$

$$\lambda^{(n)} \mathbf{W}^{(n)} = \mathbf{U}^{(n)} \mathbf{F} \quad (5)$$

Finally, the eigenvalues can be used to evaluate the relative “energy”, τ_n , of the
 n -th POD mode as

$$\tau_n = \frac{(\lambda^{(n)})^2}{\sum_m (\lambda^{(m)})^2}. \quad (6)$$

142 The most important property of the POD (that can be chosen as a definition) is
 143 the fact that modes can be ordered in terms of their significance for representing the

† We use a standard definition of the Euclidean vector norm $\|\mathbf{A}\| = \sqrt{\mathbf{A} \cdot \mathbf{A}}$, where \mathbf{A} is a vector of
 any finite dimension.

144 data. Then, one may retain only a very small number of those modes to approximate
 145 the original response. Both $\mathbf{U}^{(n)}$ and $\mathbf{W}^{(n)}$ as well as the number, $N \ll N_\delta$, of those
 146 retained modes are determined so that the norm of the difference between left and right
 147 hand side terms of Eq. (2) is minimized for any choice of N .

From the algorithmic point of view, $\lambda^{(n)}$ appear as eigenvalues sorted in descending
 order, whereas either $\mathbf{U}^{(n)}$ or $\mathbf{W}^{(n)}$ are the associated eigenvectors. Hence, the
 truncation of the above relation (Eq. 2) after the first $N < N_\delta$ modes,

$$\tilde{\mathbf{F}}_N \equiv \sum_{n=1}^N \lambda^{(n)} \mathbf{U}^{(n)}(\mathbf{x}) \mathbf{W}^{(n)}(\delta), \quad (7)$$

148 provides the best approximation of the original data in a least squares sense for a given
 149 number of modes. As a result, the POD offers a simple way of compressing the data to
 150 a low dimensional space, while guaranteeing the optimality (or minimal loss) of such an
 151 approximation.

To estimate the accuracy of the approximate description obtained by the POD
 truncation, conventionally the residual ρ_i at every spatial position \mathbf{x}_i can be computed
 as

$$\rho_i(\mathbf{x}_i) \equiv \rho_i = \frac{\sum_{j=1}^{N_\delta} (F_{ij} - (\tilde{F}_N)_{ij})^2}{\sum_{j=1}^{N_\delta} (F_{ij})^2}, \quad i = 1, \dots, N_x. \quad (8)$$

152

153 4. Patch-test: LDPE nano deposits on a PS film

154 First, a sample made from low density polyethylene (LPDE) well-separated nanopods
 155 deposited on a polystyrene (PS) substrate is considered (Fig. 2)§. This sample serves
 156 as a patch test in our work since it is commonly used to calibrate AFM tips (RTESPA-
 157 150 type). For the patch-test, a ROI area of $S = 5 \times 5 \mu\text{m}^2$ is scanned with a spatial
 158 resolution of 64×64 points and a frequency of acquisition 2 kHz.

159 Fig. 2b shows the force-indentation response for twenty random selected pixels
 160 inside the ROI. It is clear that the corresponding force-indentation response can be
 161 divided into two main data-groups: the first one exhibits a stiff response with low
 162 adhesion and negligible viscosity, whereas the second one shows a softer response and
 163 with high adhesion and viscosity (as indicated by the hysteresis during unloading).

164 It is essential to point out that even if the PF-QNM mode is controlled to reach a
 165 predefined maximum contact force, this is in practice unattainable, as the scan frequency
 166 and the complex topography prevent this condition from being accurately satisfied. As
 167 a consequence, neither the force range nor the indentation interval are kept constant

§ The SEM image does not correspond exactly to the area analyzed by the AFM. Yet, it validates
 qualitatively the AFM results.

168 from pixel to pixel, and thus, for a fair comparison of responses at different pixels, one
 169 must crop the raw recorded data to a well defined indentation or force level.

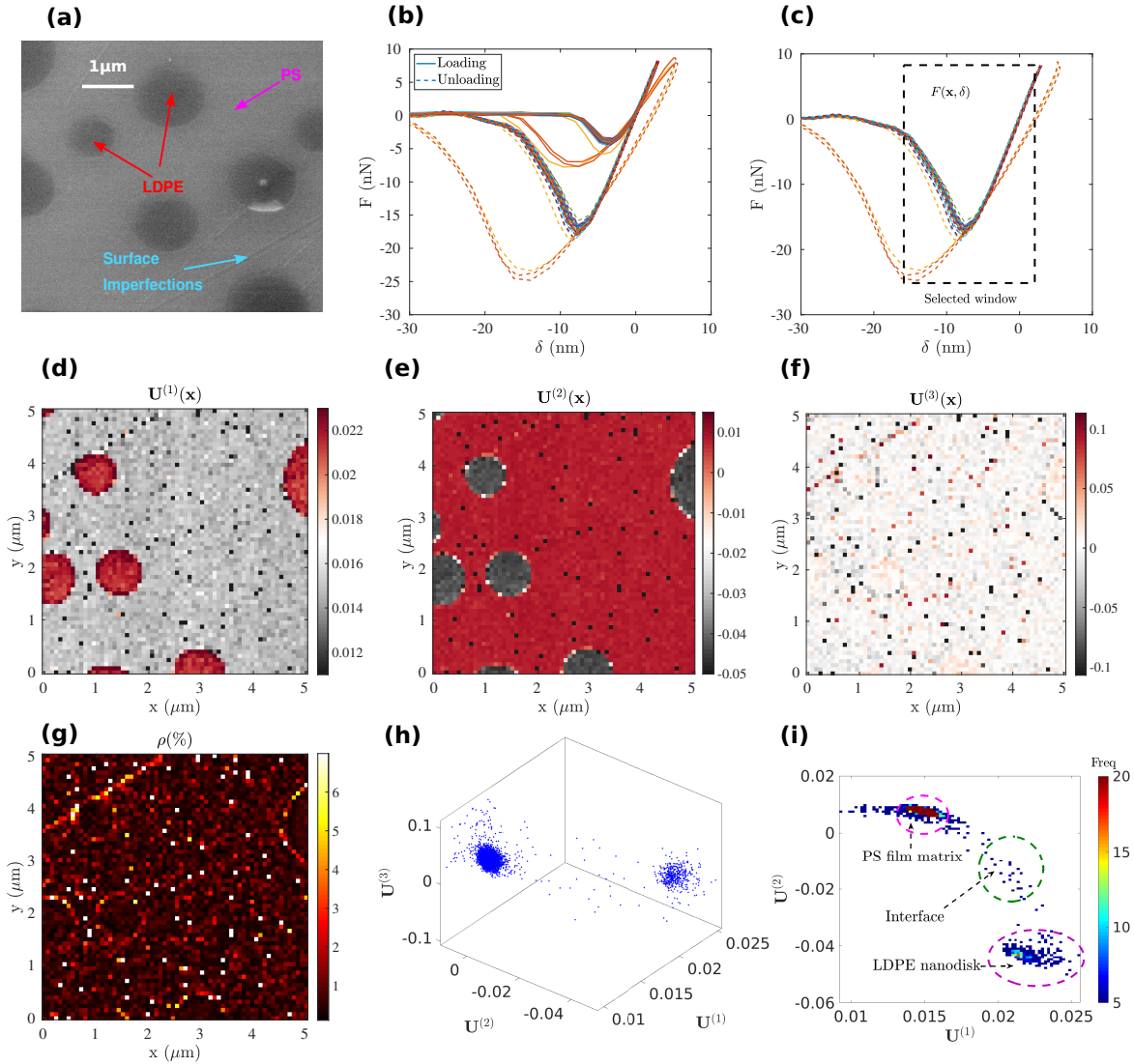


Figure 2: (a) SEM image showing LDPE nanodisks deposited on PS substrate and surface imperfections. (b) Arbitrarily selected force-indentation response at various pixels (continuous lines represent tip approach and dashed lines tip retraction). (b) Force-indentation curve during retraction; the rectangle indicates the region selected for POD analysis. (d) First POD mode spatial mode revealing the phases (e) Second POD mode revealing more subtle information such as PS-LPDE interfaces. (c) Third POD mode showing higher order features related to surface roughness. (g) Residual error resulting by keeping only the first three modes to describe the force-indentation response at each pixel. (h) Subspace generated by the first three POD modes $[\mathbf{U}^{(1)}; \mathbf{U}^{(2)}; \mathbf{U}^{(3)}]$. (i) Contour of the frequency of points in the subspace $[\mathbf{U}^{(1)}, \mathbf{U}^{(2)}]$.

170 In this regard, for the patch test, the force-indentation response is analyzed
 171 only during unloading, i.e., Regime III, as shown by the cropping window in Fig. 2c
 172 (approximately $-15 \text{ nm} \lesssim \delta \lesssim 5 \text{ nm}$. The contact response is initially (visco)elastic

173 and subsequently adhesive between the tip and the sample. This implies that our phase
 174 segmentation is done for this specific part of the $F - \delta$ response and has to be interpreted
 175 as such.

176 Subsequently, the cropped force-indentation data points are decomposed into N
 177 POD (proper orthogonal decomposition) modes as described by Eq. (7). We show next
 178 that the first few POD modes can reproduce most of the complete $F - \delta$ response by
 179 evaluating the relative power of each POD mode τ_n in the original data is evaluated via
 180 Eq. (8).

181 Fig. 2(d-f) shows the first three POD spatial modes $\mathbf{U}^{(n)}(\mathbf{x}_i), n \leq 3$, ranked
 182 from higher to lower value of τ_n . These first three POD modes represent 96% of
 183 the original measured $F - \delta$ response, leading respectively to the values, $\tau_1 = 0.75$,
 184 $\tau_2 = 0.17$, and $\tau_3 = 0.04$. The first POD mode $\mathbf{U}^{(1)}$ captures remarkably well the phase
 185 distributions (PS in gray and LDPE in light red in Fig. 2d) as the primary information
 186 of the mechanical response. The second mode, $\mathbf{U}^{(2)}$, (Fig. 2e) reveals the next level of
 187 information. In particular, light gray areas at the PS-LPDE interfaces indicates that
 188 the mechanical properties in those regions are somewhat different. Finally, the third
 189 mode $\mathbf{U}^{(3)}$ describes even higher order information that do not affect the first order
 190 effects such as the contact laws and material stiffness (Fig. 2f). For instance, the $\mathbf{U}^{(3)}$
 191 map reveals regions with steep slopes, such as a scratch at the north-west side, which
 192 correlates well with similar defects revealed in the SEM image (Fig. 2a).

193 The contributions of higher POD modes, $n > N$, are negligible as compared to the
 194 first three ones and lead mostly to a pure noise map. In this view, the residual ρ can
 195 be computed, to highlight pixels where the mechanical response is not very accurately
 196 accounted for with the number of POD modes used (Fig. 2g). For a more quantitative
 197 analysis, Fig. 2h shows the distribution of data in the subspace $[\mathbf{U}^{(1)}; \mathbf{U}^{(2)}; \mathbf{U}^{(3)}]$, where
 198 pixels are grouped into clusters. This allows the segmentation of the different phases and
 199 the identification of one or more interfacial regions. Focusing further in the subspace
 200 $[\mathbf{U}^{(1)}; \mathbf{U}^{(2)}]$ (Fig. 2i), a 2D-histogram shows the statistical frequency of points having a
 201 given value of $\mathbf{U}^{(1)}$ and $\mathbf{U}^{(2)}$. Two main phases characterized by their mean response and
 202 deviations are very clearly highlighted making mechanically-based segmentation quite
 203 simple.

204 5. Carbon-Iron particles with PDMS binder

205 The second analyzed sample is a composite material consisting of a polymer matrix
 206 (PDMS) and mechanically stiff, fairly spherical carbonyl-iron particles (CIP) with mean
 207 radius of about $\sim 3 \mu\text{m}$. The results from the built-in QNM results are first shown
 208 in Fig. 3 to reveal the complexity of the analyzed sample. Subsequently, in Fig. 4, we
 209 analyze the data using the proposed POD method.

210 As seen in Fig. 3a obtained by SEM, the white spots represent the reflections from
 211 the CIP, whereas the surface of the composite material is marked by multiple line defects.
 212 For the AFM analysis, a surface of $50 \mu\text{m}^2$ is scanned using the PF-QNM mode with a

213 definition of 128×128 points, and a frequency of 2 kHz. The scanned region is selected
 214 intentionally such that one of the surface imperfections is present in the ROI.

215 As easily observed in Fig. 3b, and unlike the previous ideal patch-test, the variation
 216 of the force-indentation curves exhibits a continuous pattern and a marked presence of
 217 viscosity and adhesive behavior. As a consequence, it is extremely difficult to segment
 218 and identify the underlying phases via a direct pixel-to-pixel analysis. In particular,
 219 as highlighted in Fig. 3c, a marked surface imperfection is observed inside the ROI
 220 (highlighted in dark color expanding from south-west to north-east). Due to the sharp
 221 change in topography and difference in effective contact surface, at these locations,
 222 both the maximum of indentation depth and adhesion are quite different than either
 223 the PDMS or the CIP response, and thus it is likely to be misinterpreted as a third
 224 phase. In the following, the results obtained from our POD proposed approach will be
 225 shown and compared with the standard PF-QNM ones.

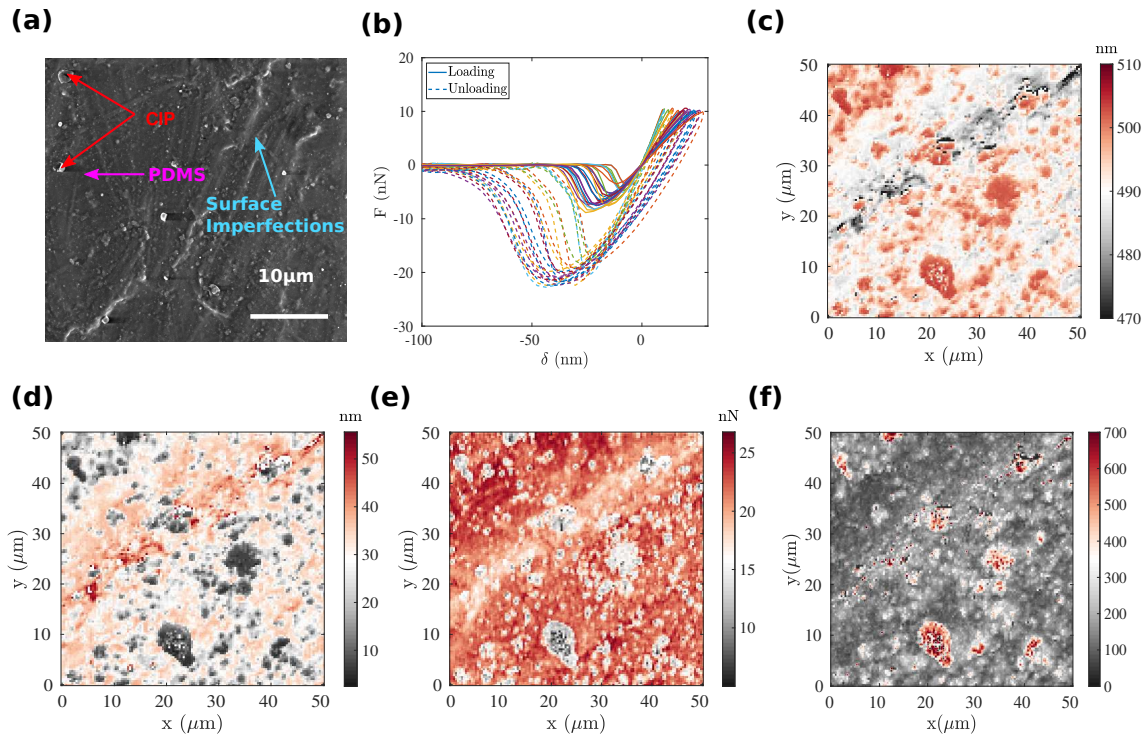


Figure 3: (a) SEM image showing carbonyl iron particles (CIP) embedded in a PDMS matrix, and surface imperfections. (b) Arbitrarily selected force-indentation response at various pixels (continuous lines represent tip approach and dashed lines tip retraction). (c) Topography map using our proposed definition; (d)-(f) Bruker's PF-QNM built-in results maximum indentation; (d) Maximum Indentation (e) Adhesion (f) Apparent modulus using Sneddon model;

226 Following the same POD procedure presented in the previous section, a window is
 227 selected in the unloading Regime III (Fig. 4a) with δ ranging from ~ -45 nm to ~ 10 nm.
 228 In this initial data-set, after the POD analysis, the first three modes are retained, as
 229 shown in Fig. 4(b-d). Their contribution amounts to $\tau_1 = 0.91 > \tau_2 = 0.04 > \tau_3 = 0.03$,
 230 respectively, describing approximately 98% of the power of the original $F - \delta$ data.

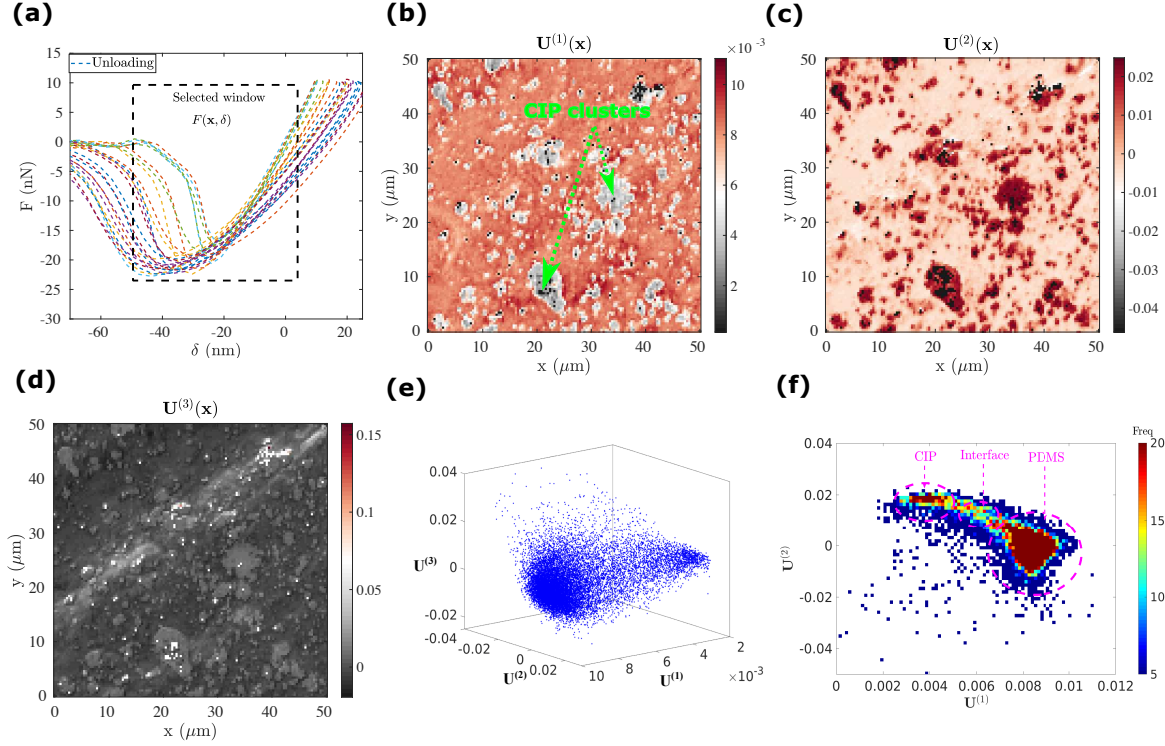


Figure 4: (a) Force-indentation curve during retraction; the rectangle indicates the region selected for POD analysis. (b)-(c) First two POD mode spatial modes revealing clearly the CIP-PDMS phases (d) Third POD mode showing higher order features related to surface roughness. (e) Subspace generated by the first three POD modes $[\mathbf{U}^{(1)}; \mathbf{U}^{(2)}; \mathbf{U}^{(3)}]$. (f) 2D histogram of amplitudes in the subspace $[\mathbf{U}^{(1)}, \mathbf{U}^{(2)}]$.

231 Remarkably, despite the continuous pattern in the $F - \delta$ responses (Fig. 4a), the
 232 first mode $\mathbf{U}^{(1)}$ (Fig. 4b) reveals the presence of the PDMS matrix (in red) contrasting
 233 with the much smaller amplitude of the stiff CIP phase (in white). In particular, we
 234 observe a pronounced clustering of CIP particles in at least four regions that exceed a
 235 side length of $10 \mu\text{m}$ (i.e., 3-4 times the radius if the particle) due to aggregation during
 236 the sample fabrication. Fig. 4b illustrates the strength of the AFM-POD analysis as
 237 compared with the SEM imaging, wherein such delicate features are much more difficult
 238 to obtain.

239 The second mode (Fig. 4c) in the present case does not exhibit substantially
 240 different features than the first one. In fact, one may note that the CIP particles
 241 now have a much larger weight than the soft matrix, *i.e.* opposite to the case of the first
 242 mode. With our proposed algorithm, the rough surface topography does not appear to
 243 bias the phase contrast seen in Fig. 4b and c. By contrast, the surface topography is
 244 mingled with the phase contrast in all the different Bruker outputs in Fig. 3. Thus, it
 245 may be concluded that in the present examples, the POD analysis is a trustworthy and
 246 efficient method for phase segmentation.

247 Finally, the third mode (Fig. 4d) reveals the next order of information, this time
 248 highlighting the aforementioned topographical defect (light white color) ranging from

south-west to north-east. In the literature, the influence of topography on apparent
 adhesion has been intensively studied. A sharp variation in surface curvature often leads
 to a decrease in adhesion for the same material [39]. This observation is consistent with
 the results reported here as well as those processed by the Bruker AFM software, in spite
 of the fact that the first modes were observed to be independent of topography. Hence,
 the POD analysis appears to be an efficient method for rearranging hierarchically and
 separately different features in PF-QNM AFM data (phase, topography) according to
 their contribution in the mechanical signal, allowing analysts to describe each individual
 aspects or their combination altogether.

Focusing, next, on the reduced subspace $[\mathbf{U}^{(1)}; \mathbf{U}^{(2)}; \mathbf{U}^{(3)}]$ allows to reveal the
 continuous distribution of the data (Fig. 4e). Given that topography is almost
 entirely suppressed in the first two POD modes, the subspace $[\mathbf{U}^{(1)}; \mathbf{U}^{(2)}]$, (Fig. 4f),
 becomes a natural “best-candidate” for the purpose of phase segmentation. Two distinct
 peaks, corresponding to the two main phases, i.e, PDMS and CIP can be observed.
 However, the scatter of points and the overlap of the two domains suggests in this
 case that the transition (in terms of apparent mechanical properties) is progressive. It
 may be speculated that particles buried at different depth beneath the surface may be
 responsible for this observation.

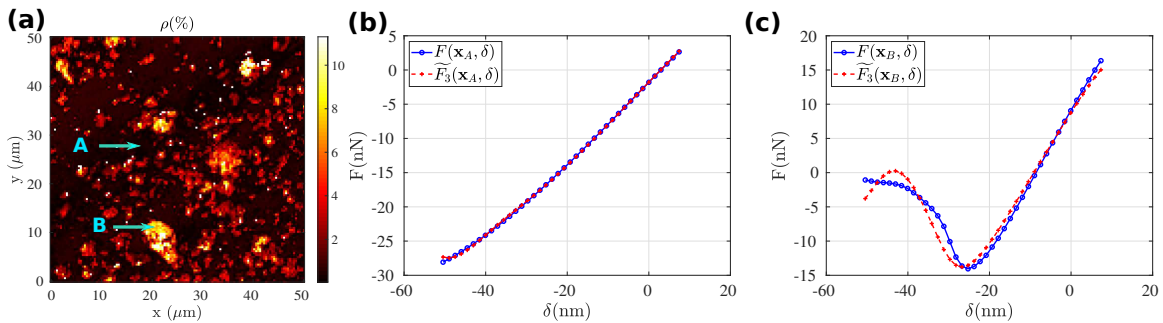


Figure 5: Uncertainty(residual) of reconstruction using the first three POD modes: (a) The residual map ; (b) Comparison between the initial force-indentation curve (plotted in dot blue) and reconstructed curve (plotted in red) at point A ($\rho(\mathbf{x}_A) \simeq 1\%$); (c) Comparison between the initial force-indentation curve (plotted in dot blue) and reconstructed curve (plotted in red) at point B ($\rho(\mathbf{x}_B) \simeq 10\%$)

Finally, in order to assess the accuracy of the POD reconstruction, we show in
 Fig. 5a, the residual, ρ , which serves to measure the error induced by the truncation
 to only the first three modes at each pixel. This measure suggests that CIP clusters
 may require a finer analysis to be better described. In particular, we select and analyze
 two points with different residual levels, as shown in Fig. 5a. At point A located in
 the PDMS matrix (see Fig. 5b), the initial force curve is perfectly reconstructed with
 an error that is less than 1%. In contrast, at point B located inside a cluster of CIP
 particles, (Fig. 5c), the truncation error (of the order of $\simeq 10\%$) is mostly concentrated
 at the maximum pull-out force. One possible explanation is that the error results from
 the unstable mechanism of ‘snap-off’ between tip and sample. However, the hysteretic

277 mechanism of 'snap-off' is out of the scope of this study, and thus we did not further
278 attempt to reduce the reconstruction error by introducing additional higher order POD
279 modes.

280 6. Conclusions

281 Accessing complex nano- and microstructural morphologies in heterogeneous media is
282 both a need and a challenge. The recent PF-QNM AFM mode represents a major step
283 forward to provide such fine information, whereby each image pixel is fully characterized
284 by a complete mechanical test. However, the analysis of the resulting large data-sets
285 becomes not only delicate (because of the intrinsic coupling of different mechanical
286 and chemical properties with the topography), but also time-wise prohibitive. This
287 letter has shown that model reduction techniques (such as the POD), can be extremely
288 useful in organizing hierarchically such large data-sets allowing not only to identify
289 a small number of modes expressing the underlying phases but also to offer an easy
290 segmentation of the (mechanically relevant) phases. Starting from the force-indentation
291 response, proper classification may reveal discrete material responses, allowing to extract
292 seamlessly the mechanical, chemical or physical response of each of them. In materials
293 with complex microstructures, the proposed processing may indicate, at first sight,
294 that mechanical properties are continuously varying making a manual identification
295 impossible. The POD method allows to properly identify the data points belonging to
296 the same phase and possibly to a transition region between them.

297 We close by emphasizing that the agnostic character of the data processing
298 techniques used here is both a strength — no bias is introduced by enforcing say a
299 contact model that would be unsuited — and a weakness — the physical interpretation
300 (*e.g.* elastic stiffness, adhesive properties, viscoelasticity) remains in the hand of the
301 user. However, this interpretation becomes now substantially easier and more robust
302 since only a reduced subspace of a much lower dimensionality (*i.e.* modes) needs to be
303 considered.

304 Acknowledgement

305 X.C., S.H. and K.D. would like to thank Becton and Dickinson Corporation (BD) for
306 financing partially this project and Ms. Saphia Ouanani from Bruker Corporation for
307 very useful discussions. K.D. would also like to acknowledge partial support from the
308 European Research Council (ERC) under the European Union's Horizon 2020 research
309 and innovation program (grant agreement No 636903).

310 **Appendix A. PS-LDPE sample**311 *Appendix A.1. Description of the sample*

312 The detailed information concerning the sample type PS-LDPE-12M can be found at the
 313 following address: <https://www.brukerafmprobes.com/p-3724-ps-ldpe-12m.aspx>

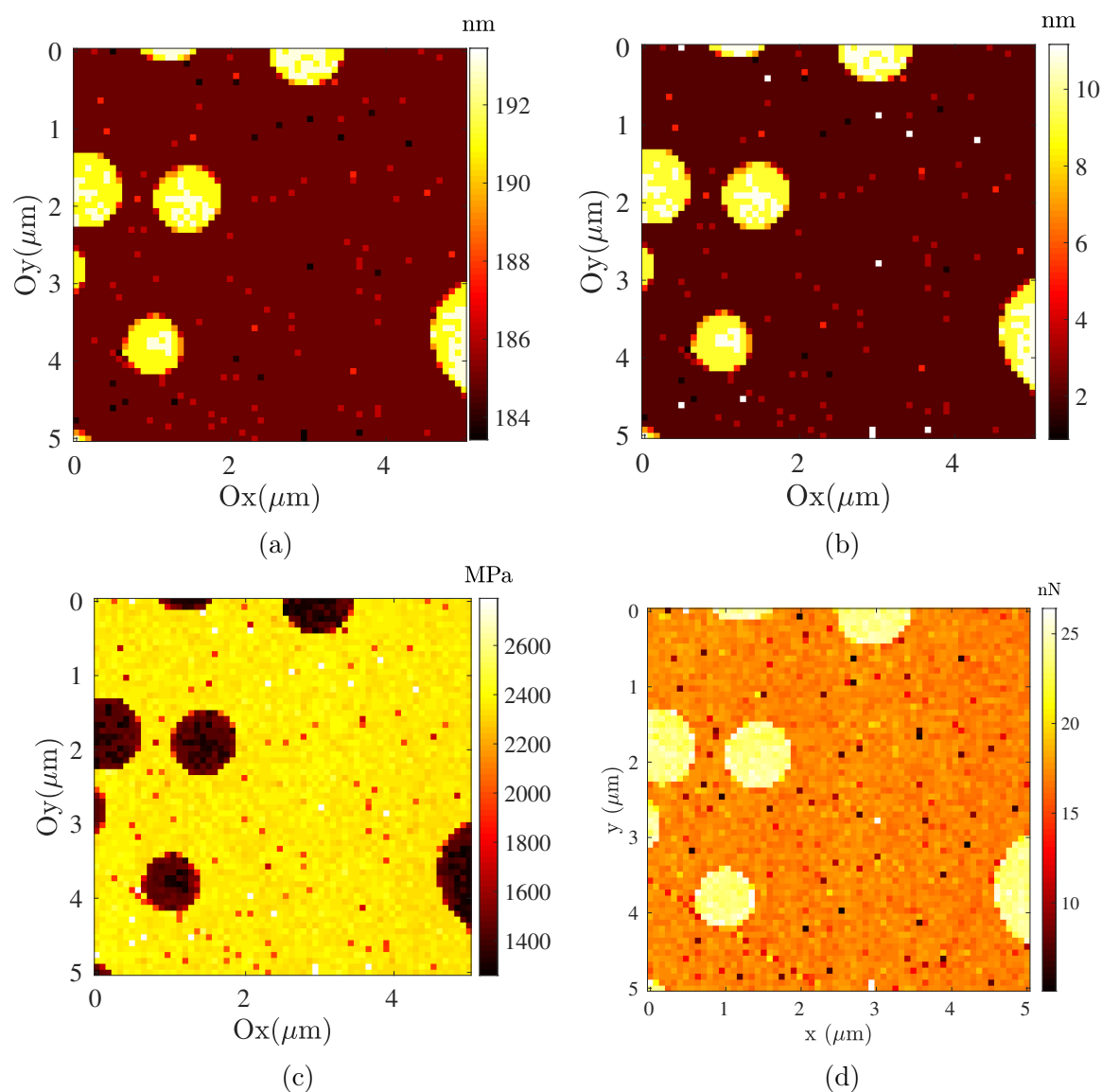
314 *Appendix A.2. QNM properties*

Figure A1: The PF-QNM modality proposed by Bruker provides different mechanical characterizations based on the AFM scan discussed in the main text of the manuscript, relative to the PS-LDPE sample. (a) Topography map; (b) Maximum indentation; (c) Apparent modulus using Hertz model; (d) Adhesion

315 Appendix A.3. SEM image

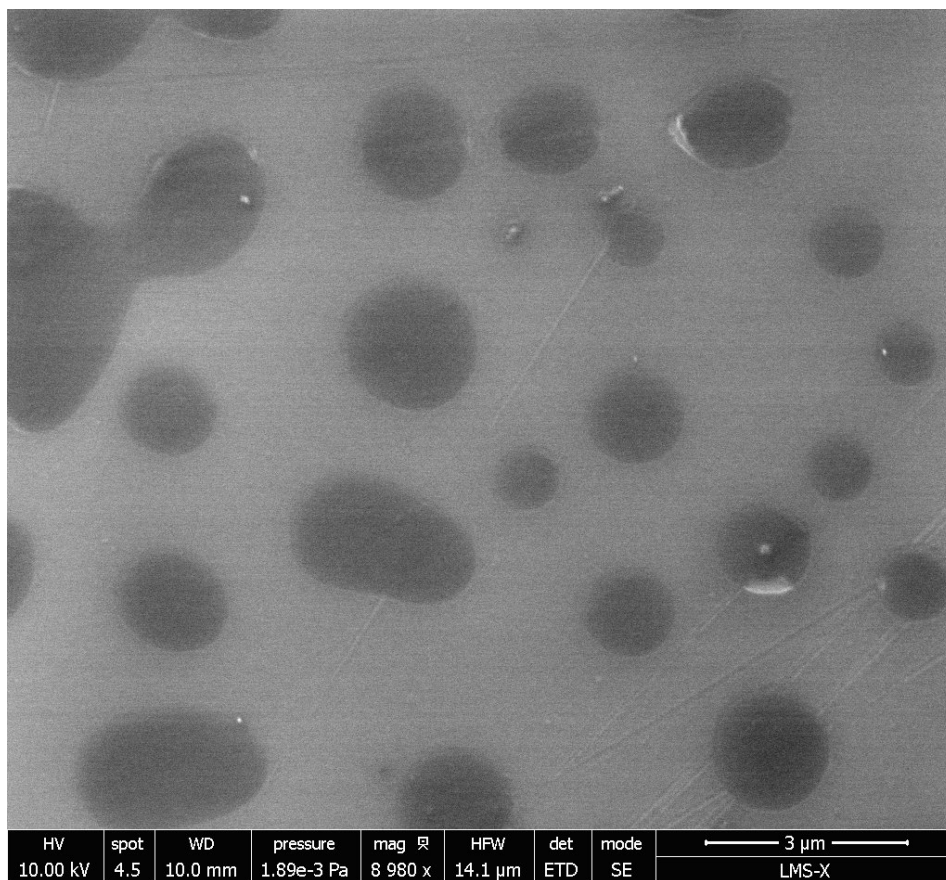


Figure A2: SEM image (secondary electrons) for the PS-LDPE sample (the dark gray domains are the LDPE nanopods while the PS film substrate appears in light gray)

316 **Appendix B. PDMS-CIP sample**317 *Appendix B.1. Fabrication process*

318 The fabrication procedure of the PDMS+CIP composite can be summarized as follows
319 (see more details in [34]):

- 320 1. The appropriate amount of CIP powder is mixed along with part A + part B (10:1)
321 of Sylgard 184 in a beaker.
- 322 2. All ingredients are thoroughly mixed for two minutes at 200 RPM mixer.
- 323 3. The mixture is put into a vacuum chamber for 34 minutes to remove the entrapped
324 air.
- 325 4. The degassed liquid mixture is put in an aluminum mold.
- 326 5. The mold is heated in an oven at temperature $T = 373$ K for two hours.

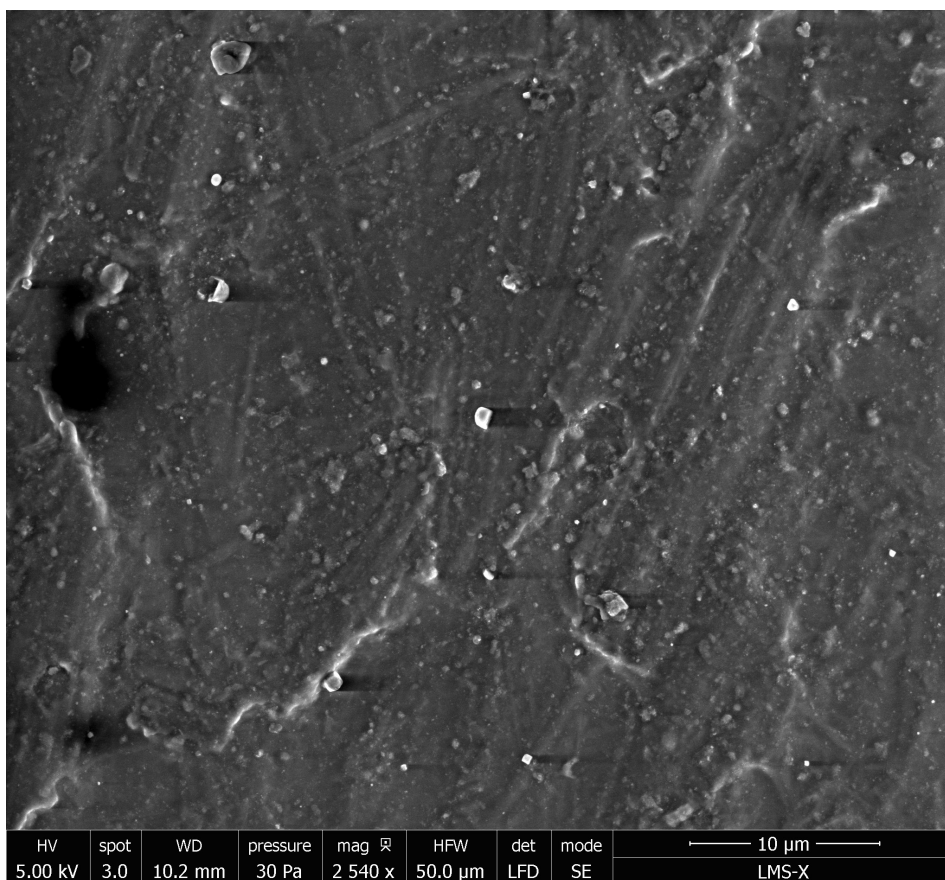
327 *Appendix B.2. SEM image*

Figure B1: SEM image (secondary electrons) for the PDMS-CIP sample. Bright spots originates from the Carbonyl-Iron particles, while the PDMS shows a darker gray level. A significant roughness of the surface is visible

328 **Appendix C. POD truncation**

Note that \mathbf{F} by construction is not a square (and hence not symmetric). In order to accelerate the computations, we symmetrize \mathbf{F} in order to form a square matrix of a minimum dimension that allows to obtain seamlessly the eigenvalues $\lambda^{(n)}$ and the eigenvectors $\mathbf{W}^{(n)}$. In the present work, we always have $N_\delta < N_x$. As a consequence, the most efficient symmetrization is obtained by setting [30],

$$\mathbf{M} = \mathbf{F}^T \mathbf{F}, \quad \text{or} \quad M_{ij} = \sum_{k=1}^{N_x} F_{kj} F_{ki}. \quad (\text{C.1})$$

This operation leads to a matrix \mathbf{M} of size $N_\delta \times N_\delta$. The alternative one $\mathbf{F} \cdot \mathbf{F}^T$ would lead to a matrix size of dimension $N_x \times N_x > N_\delta \times N_\delta$. Using now the definition introduced in Eq. (2) and simple linear algebra, we can readily get

$$M_{ij} = \sum_{n=1}^{N_\delta} (\lambda^{(n)})^2 W_i^{(n)} W_j^{(n)}. \quad (\text{C.2})$$

329 Thus, use of the symmetric (square) matrix \mathbf{M} instead of the non-symmetric \mathbf{F} allows to
 330 extract in a very simple manner the eigenvalues $\lambda^{(n)}$ and eigenvectors $\mathbf{W}^{(n)}$ by employing
 331 any eigensystem algorithm for symmetric real matrices. Once those two quantities are
 332 evaluated, one may extract the remaining spatial modes $\mathbf{U}^{(n)}$ by use of the orthogonality
 333 between the $\mathbf{W}^{(n)}$ modes and the direct projection operation, described in Eq. (4).

334 The following algorithm describes the POD operations using this last definition as
 335 well as the definitions in Section 3.

Algorithm 1: POD truncation

Result: Compute N force and spatial modes using POD

Crop Force \mathbf{F} and indentation $\boldsymbol{\delta}$ data to selected range;

Resample $(\mathbf{F}, \boldsymbol{\delta})$ using linear interpolation to a prescribed number of δ points;

Force data for all pixels i and δ_j sampling to be gathered into a matrix F_{ij} ;

Compute the square symmetric matrix $\mathbf{M} = \mathbf{F}^T \mathbf{F}$;

Extract the eigenvalues $\lambda^{(n)}$ of \mathbf{M} sorted in decreasing order and the
 corresponding eigenvectors $\mathbf{W}^{(n)}$ with $n = 1, \dots, N_\delta$;

Select the appropriate number of modes $N \ll N_\delta$ from the eigenvalue
 spectrum;

Compute the corresponding spatial mode $\mathbf{U}^{(n)} = \frac{1}{\lambda^{(n)}} \mathbf{F} \mathbf{W}^{(n)}$ with $n = 1, \dots, N$;

- 336 [1] G. Binnig, C. F. Quate, and Ch. Gerber. Atomic force microscope. *Phys. Rev. Lett.*, 56:930–933,
337 Mar 1986.
- 338 [2] C.F Quate. The afm as a tool for surface imaging. *Surface Science*, 299-300:980 – 995, 1994.
- 339 [3] S.N. Magonov, V. Elings, and M.-H. Whangbo. Phase imaging and stiffness in tapping-mode
340 atomic force microscopy. *Surface Science*, 375(2):L385 – L391, 1997.
- 341 [4] A Rosa-Zeiser, E Weilandt, S Hild, and O Marti. The simultaneous measurement of elastic,
342 electrostatic and adhesive properties by scanning force microscopy: pulsed-force mode operation.
343 *Measurement Science and Technology*, 8(11):1333–1338, nov 1997.
- 344 [5] Lining Lan, Shuhong Xie, Li Tan, and Jiangyu Li. Sol-gel based soft lithography and piezoresponse
345 force microscopy of patterned pb(zrti) microstructures. *Journal of Materials Science &
346 Technology*, 26(5):439 – 444, 2010.
- 347 [6] D. Passeri, M. Rossi, and J.J. Vlassak. On the tip calibration for accurate modulus measurement
348 by contact resonance atomic force microscopy. *Ultramicroscopy*, 128:32 – 41, 2013.
- 349 [7] T J Young, M A Monclus, T L Burnett, W R Broughton, S L Ogin, and P A Smith. The
350 use of the PeakForceTMquantitative nanomechanical mapping AFM-based method for high-
351 resolution young's modulus measurement of polymers. *Measurement Science and Technology*,
352 22(12):125703, oct 2011.
- 353 [8] Kim K. M. Sweers, Kees O. van der Werf, Martin L. Bennink, and Vinod Subramaniam. Atomic
354 force microscopy under controlled conditions reveals structure of c-terminal region of α -synuclein
355 in amyloid fibrils. *ACS Nano*, 6(7):5952–5960, 2012. PMID: 22695112.
- 356 [9] Maxim E. Dokukin and Igor Sokolov. Quantitative mapping of the elastic modulus of soft materials
357 with harmonix and peakforce qnm afm modes. *Langmuir*, 28(46):16060–16071, 2012. PMID:
358 23113608.
- 359 [10] Moritz Pfreundschuh, David Alsteens, Manuel Hilbert, Michel O. Steinmetz, and Daniel J. Müller.
360 Localizing chemical groups while imaging single native proteins by high-resolution atomic force
361 microscopy. *Nano Letters*, 14(5):2957–2964, 2014. PMID: 24766578.
- 362 [11] Hsien-Shun Liao, Ka Kit Lei, and Yu Fang Tseng. High-speed force mapping based on an
363 astigmatic atomic force microscope. *Measurement Science and Technology*, 30(2):027002, jan
364 2019.
- 365 [12] Franz J. Giessibl. Advances in atomic force microscopy. *Rev. Mod. Phys.*, 75:949–983, Jul 2003.
- 366 [13] Yueming Hua. PeakForce-QNM advanced applications training 2014. *Technical Support Engineer*,
367 2012.
- 368 [14] G. Smolyakov, S. Pruvost, L. Cardoso, B. Alonso, E. Belamie, and J. Duchet-Rumeau. Afm
369 peakforce qnm mode: Evidencing nanometre-scale mechanical properties of chitin-silica hybrid
370 nanocomposites. *Carbohydrate Polymers*, 151:373 – 380, 2016.
- 371 [15] Laida Cano, Daniel Humberto Builes, Sheyla Carrasco-Hernandez, Junkal Gutierrez, and
372 Agnieszka Tercjak. Quantitative nanomechanical property mapping of epoxy thermosetting
373 system modified with poly(ethylene oxide-b-propylene oxide-b-ethylene oxide) triblock
374 copolymer. *Polymer Testing*, 57:38 – 41, 2017.
- 375 [16] M. Majewska, D. Mrdenovic, I.S. Pieta, R. Nowakowski, and P. Pieta. Nanomechanical
376 characterization of single phospholipid bilayer in ripple phase with pf-qnm afm. *Biochimica
377 et Biophysica Acta (BBA) - Biomembranes*, 1862(9):183347, 2020.
- 378 [17] E. Barthel and S. Roux. Velocity-dependent adherence: An analytical approach for the jkr and
379 dmt models. *Langmuir*, 16(21):8134–8138, 2000.
- 380 [18] Gregory D. Jay, Jahn R. Torres, David K. Rhee, Heikki J. Helminen, Mika M. Hytinen, Chung-
381 Ja Cha, Khaled Elsaid, Kyung-Suk Kim, Yajun Cui, and Matthew L. Warman. Association
382 between friction and wear in diarthrodial joints lacking lubricin. *Arthritis & Rheumatism*,
383 56(11):3662–3669, 2007.
- 384 [19] Qunyang Li and Kyung-Suk Kim. Micromechanics of friction: effects of nanometre-scale
385 roughness. *Proceedings of the Royal Society A: Mathematical, Physical and Engineering
386 Sciences*, 464(2093):1319–1343, 2008.

- 387 [20] Uzi Landman, W. D. Luedtke, Nancy A. Burnham, and Richard J. Colton. Atomistic mechanisms
388 and dynamics of adhesion, nanoindentation, and fracture. *Science*, 248(4954):454–461, 1990.
- 389 [21] N.A. Fleck, G.M. Muller, M.F. Ashby, and J.W. Hutchinson. Strain gradient plasticity: Theory
390 and experiment. *Acta Metallurgica et Materialia*, 42(2):475 – 487, 1994.
- 391 [22] William D. Nix and Huajian Gao. Indentation size effects in crystalline materials: A law for strain
392 gradient plasticity. *Journal of the Mechanics and Physics of Solids*, 46(3):411 – 425, 1998.
- 393 [23] G. Haiat, M.C. Phan Huy, and E. Barthel. The adhesive contact of viscoelastic spheres. *Journal*
394 *of the Mechanics and Physics of Solids*, 51(1):69 – 99, 2003.
- 395 [24] E Barthel. Adhesive elastic contacts: Jkr and more. *Journal of Physics D: Applied Physics*,
396 41:163001, 2008.
- 397 [25] David Lin, Emiliios Dimitriadis, and Ferenc Horkay. Robust strategies for automated afm force
398 curve analysis—i. non-adhesive indentation of soft, inhomogeneous materials. *Journal of*
399 *biomechanical engineering*, 129:430–40, 07 2007.
- 400 [26] David Lin, Emiliios Dimitriadis, and Ferenc Horkay. Robust strategies for automated afm
401 force curve analysis—ii: Adhesion-influenced indentation of soft, elastic materials. *Journal*
402 *of biomechanical engineering*, 129:904–12, 01 2008.
- 403 [27] David C. Lin, David I. Shreiber, Emiliios K. Dimitriadis, and Ferenc Horkay. Spherical indentation
404 of soft matter beyond the hertzian regime: numerical and experimental validation of hyperelastic
405 models. *Biomechanics and Modeling in Mechanobiology*, 8(5):345, Nov 2008.
- 406 [28] B J Briscoe, L Fiori, and E Pelillo. Nano-indentation of polymeric surfaces. *Journal of Physics*
407 *D: Applied Physics*, 31(19):2395–2405, oct 1998.
- 408 [29] Michel Verleysen and Damien François. The curse of dimensionality in data mining and time series
409 prediction. volume 3512, pages 758–770, 06 2005.
- 410 [30] Anindya Chatterjee. An introduction to the proper orthogonal decomposition. *Current science*,
411 pages 808–817, 2000.
- 412 [31] Charles F Van Loan. Generalizing the singular value decomposition. *SIAM Journal on numerical*
413 *Analysis*, 13(1):76–83, 1976.
- 414 [32] Svante Wold, Kim Esbensen, and Paul Geladi. Principal component analysis. *Chemometrics and*
415 *intelligent laboratory systems*, 2(1-3):37–52, 1987.
- 416 [33] K. Danas, S.V. Kankanala, and N. Triantafyllidis. Experiments and modeling of iron-particle-
417 filled magnetorheological elastomers. *Journal of the Mechanics and Physics of Solids*, 60(1):120
418 – 138, 2012.
- 419 [34] L. Bodelot, J.-P. Voropaieff, and T. Pössinger. Experimental investigation of the coupled magneto-
420 mechanical response in magnetorheological elastomers. *Experimental Mechanics*, 58(2):207–221,
421 sep 2017.
- 422 [35] Erato Psarra, Laurence Bodelot, and Kostas Danas. Two-field surface pattern control via
423 marginally stable magnetorheological elastomers. *Soft Matter*, 13(37):6576–6584, 2017.
- 424 [36] E. Psarra, L. Bodelot, and K. Danas. Wrinkling to crinkling transitions and curvature localization
425 in a magnetoelastic film bonded to a non-magnetic substrate. *Journal of the Mechanics and*
426 *Physics of Solids*, 133:103734, 2019.
- 427 [37] Sebastian Rützel, Soo Il Lee, and Arvind Raman. Nonlinear dynamics of atomic force microscope
428 probes driven in lennard jones potentials. *Proceedings of the Royal Society of London. Series*
429 *A: Mathematical, Physical and Engineering Sciences*, 459(2036):1925–1948, 2003.
- 430 [38] K. K. Nomura and S. E. Elghobashi. The structure of inhomogeneous turbulence in variable
431 density nonpremixed flames. *Theoretical and Computational Fluid Dynamics*, 5(4):153–175,
432 Nov 1993.
- 433 [39] T. Stifter, E. Weilandt, O. Marti, and S. Hild. Influence of the topography on adhesion measured
434 by sfm. *Applied Physics A*, 66(1):S597–S605, Mar 1998.